Cost and time-efficient microdevice fabrication process for rarefied gas flow applications

Nicolas Gaignebet, Marcos Rojas-Cárdenas, Stéphane Colin, Simon Raffy, Matthieu Raison, Étienne Palleau

Cost and time-efficient micro-device fabrication process for rarefied gas flows applications

Nicolas Gaignebet,[1,2,3] Marcos Rojas-Cárdenas,[1,2] * Stéphane Colin,[1,2] Simon Raffy,[2,3] Matthieu Raison,[4] and Étienne Palleau[2,3]

[1)]*Institut Clément Ader (ICA), CNRS, INSA Toulouse, ISAE-SUPAERO, IMT Mines Albi, Université Toulouse 3 Paul Sabatier, 3 rue Caroline Aigle, 31400 Toulouse, France*

[2)]*Research Federation FR3089 FERMaT (Fluids, Energy, Reactors, Materials and Transferts), CNRS, ONERA, INSA Toulouse, INP Toulouse, Université Toulouse 3 Paul Sabatier, INRAE, 4 Allée Émile Monso, 31432 Toulouse CEDEX 4, France*

[3)]*Laboratory of Physics and Chemistry of Nano-Objects (LPCNO), CNRS, INSA Toulouse, Université Toulouse 3 Paul Sabatier, 135 Avenue de Rangueil, 31077 Toulouse, France*

[4)]*Microlight3D, 5 Avenue du Grand Sablon, 38700 La Tronche, France*

(*Electronic mail: marcos.rojas@insa-toulouse.fr)

(Dated: November 23, 2024)

This study presents a rapid and cost-effective method for fabricating microchannels for rarefied gas flows applications using maskless photolithography. The geometrical characteristics of the micro-channels were characterized via optical microscopy and profilometry, while their fluidic performances were characterized for gas flows at varying levels of rarefaction. The fluid conductance of the fabricated microchannels was measured and compared with theoretical predictions, demonstrating excellent agreement thus confirming the precision of the fabrication process. Our findings indicate that the microchannels maintain dimensional integrity across different pressure levels, validating the reliability of the chosen materials and methods. Through this research, we have established a robust, low-cost, and rapid fabrication process based on maskless photolithography for producing affordable microfluidic devices for rarefied gas flows applications.

Microchannel fabrication is a cornerstone process in the development of microfluidic systems and Micro-Electro-Mechanical-Systems (MEMS), with widespread applications in gas flow sensing,[1] biomedical diagnostics,[2] or environmental monitoring.[3] Gas flows in micro-confined environments are characterized by rarefied conditions for certain channel dimensions and flow pressures. Under rarefaction conditions, thermodynamic non-equilibrium phenomena, such as velocity and thermal slips, as well as temperature jumps at the wall, may occur.[4] Rarefaction arises when the mean free path of the gas molecules is comparable to or larger than the characteristic dimensions of the channel. However, the fabrication of microchannels with the necessary precision and dimensions to leverage rarefaction effects has traditionally been a costly and complex process, often involving sophisticated lithography and etching techniques.[5,6]

Thus, efforts have been made to propose more affordable microfabrication techniques.[7,8] In order to facilitate prototyping and versatile approaches where regular changes in design geometries are required, methods involving the production of physical masks have to be avoided. Emerging low-cost techniques, such as xurography,[9] micromilling,[10] additive manufacturing,[11] or laser ablation[12] offer promising alternatives to conventional processes. These approaches not only reduce manufacturing costs but also simplify production processes, making new applications feasible across a broader range of domains, including in resource-limited settings. However, they still face drawbacks like limited resolution (tens to hundreds of micrometers) or compatibility with certain types of materials. Nowadays, digital mask photolithography processes, often referred to as maskless photolithography processes, are gaining ground in microfabrication.[13] These techniques enable rapid and versatile production of microstructures, allowing for quick design adaptations without the delays associated with traditional physical mask creation. While challenges remain, such as achieving higher resolution in the sub-micrometer range[14] or throughput, the advantages of flexibility, reduced lead times, and the potential for complex geometries make maskless photolithography particularly appealing for the development of rarefied gas flow devices, where precise microchannel dimensions are crucial for controlling flow behavior.[4] This fabrication technique is therefore an extremely suitable candidate for developing microdevices that exploit gas flows and rarefaction phenomena, such as the Knudsen pump, which utilizes temperature gradients to macroscopically transport gas, resulting in a system without moving parts;[15–18] gas chromatography, which exploits different species relative velocities for separation[19]; and fluidic oscillators for heat management at the microscale[20].

In this article, we develop a low-cost fabrication method for microchannels using a maskless photolithography process combined with standard dry film resists. This approach enables the rapid, versatile, and cost-effective production of microchannels that are suitable for isothermal gas flows in sub-atmospheric conditions, ultimately aiming at developing an economical fabrication process for rarefied and non-rarefied flow applications. We present, for three samples, the detailed microchannels fabrication steps, their geometrical characterization to ensure dimensional accuracy, and their fluidic properties in terms of mass flow rate and fluid conductance. The experimental measurements are then compared to a theoretical model for gas flow in microchannels with rectangular cross-sections at moderate rarefaction parameters.

In this work, three different microchannel samples with same geometrical characteristics were fabricated. Traditionally, micro-scale device fabrication processes rely on lithog-

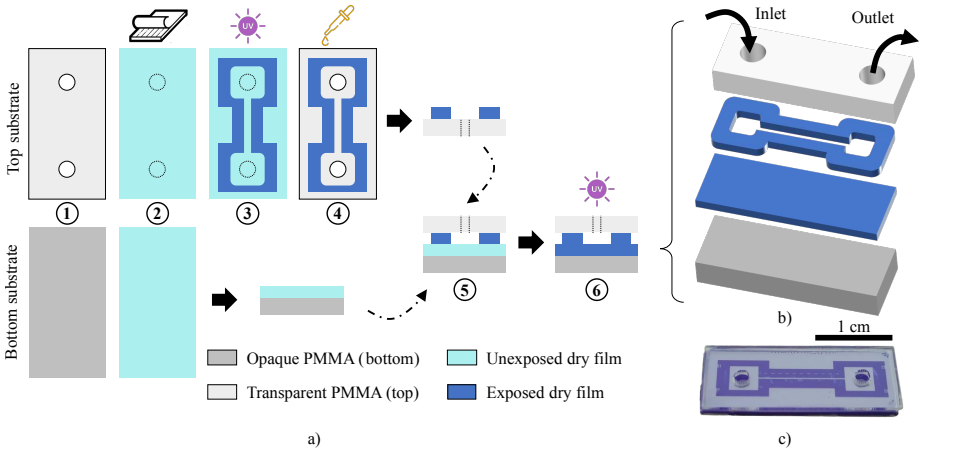

Figure 1. Schematic views of a) the fabrication process from raw materials to final chip assembly; b) the microfluidic chip with microchannel in an exploded view and c) picture of a completed chip.

raphy techniques that involve costly materials and complex steps. These typically include the use of physical masks and photosensitive resists to transfer patterns onto a substrate, followed by either etching or deposition to form the final patterned layer. The resist is usually removed afterward. This approach is widely adopted, even in low-cost photolithography processes.[21,22] However, in this study, the patterned resist itself serves as the final functional layer, eliminating the need for additional etching or deposition steps. It simplifies the fabrication process and reduces associated costs. Although this strategy has been previously proposed for the fabrication of microfluidic devices using standard photolithography,[23] to our knowledge, it has not yet been applied in the context of maskless photolithography process for rarefied gas flow applications.

For what concerns the materials involved in the process, we selected a photosensitive negative working aqueous dry film as the resist layer (LAMINAR® E9200 series from Eternal). This cost-effective photopolymer is commonly used in the integrated circuit industry and available in various thicknesses. For the substrate, we chose cast Poly(methyl methacrylate) (PMMA) due to its low cost, a thermal shape stability up to 100 °C and high surface flatness, features which are ideal for dry film lamination. Additionally, transparent PMMA allows for optical access into the fluid flow, which might be of great advantage for liquid flow characterization or optical interaction.

Maskless photolithography consists in transferring the chosen geometrical pattern to the dry film via a digital mask during the lithography step. For this process, we used the Digital Micromirror Device (DMD) technology,[24,25] which functions by projecting UV light through an array of micromirrors. The mirrors either direct the light onto the substrate or deflect it away, thereby dynamically creating a digital mask. The reflected light is focused onto the substrate using a microscope objective, with the magnification determining the achievable fabrication resolution. A simple gray scale image file is sufficient to define the pattern, eliminating the need for a physical mask, which often represents a bottleneck in microfabrication processes. This method offers a low-cost, rapid and flexible fabrication approach ideal for prototyping and fabrication of complex microstructures.

Although DMD lithography systems are commercially available, custom laboratory setups can be assembled using standard optical components,[26–28] offering a more cost-effective alternative. For this work, a Smart Print UV photolithography system from Microlight3D was used, which delivers resolutions down to a few micrometers and is capable of patterning up to 2-inch wafers surfaces. It is worth noting that depending on the targeted applications, required channel geometry and complexity, our photolithography process can be adapted to other leak-proof dry films as well as spin-coated resists if thicknesses in the sub-micrometer scale are required.

Our digital mask featuring the desired microchannel pattern was created using the free mask editor software KLayout. The digital mask features a microchannel of width $W = 200\,\mu$m and length $L = 11.5\,$mm, and two identical reservoirs with large cross-sections at the inlet and outlet of the microchannel (**Figure 1**). The reservoirs are designed overlap the inlet and outlet holes pre-cut in the top PMMA substrate. The large cross-section of the reservoirs minimizes their hydraulic resistance to gas flow. Surrounding the microchannel and reservoirs is a border approximately 1 mm wide, which reduces the remaining dry film surface to enhance adhesion and prevent bubble entrapment that could cause leakage, while retaining sufficient area to ensure a solid bond. The fabrication process is composed mainly of six different steps (**Figure 1**.a):

(1) Substrate preparation: two PMMA substrates of 26 mm×10 mm rectangular cross-section and 1 mm thickness are laser cut from a larger plate. The substrates are then

cleaned with ethanol. Two 1 mm holes are also laser cut in the top substrate to create the inlet and outlet ports.

(2) Lamination: a 50 µm-thick dry film is laminated onto both substrates using a standard PCB dry film laminator at 100 °C, with reproducible pressure and speed. This step only takes a few seconds. It is important to note that the channel height is determined by the thickness of the dry film. Dry films with other thicknesses are commercially available.

(3) UV exposure: the top dry film is exposed to UV light at a wavelength of 380 nm. The exposure process lasts around 1 min to cover the entire sample surface area (2.6 mm^2). The exposure dose is 57 $mJ\,cm^{-2}$. We use a 2.5 × magnification objective to attain the desired resolution of 6 µm, which is sufficient for our application, while keeping the total exposure time minimal.

(4) Development: the non-UV-exposed areas of the top dry film are developed in a sodium carbonate solution at 0.85 % for 3 min. The development occurs at room temperature. Next, the samples are rinsed with deionized water to remove any residual developer and dissolved dry film, ensuring a clean surface before proceeding to the sealing step.

(5) Channel sealing: the microchannel is sealed by pressing the patterned layer against the bottom PMMA substrate laminated with a plain layer of dry film. This step ensures strong adhesion between the two substrates, as the exposed dry film on the top substrate does not naturally bond to PMMA. During the sealing operation, care is taken to apply even pressure across the entire surface to avoid creating voids or uneven contact that could compromise the integrity of the microchannel. Excessive pressure can deform the unexposed dry film layer and potentially affect the channel dimensions. The pressure is maintained for a few seconds, after which the assembly is carefully inspected for any visible defects. Imperfectly bonded areas are visible to the naked eye, as defects like bubbles and dust create gaps between the dry film layers, resulting in detectable reflections.

(6) Final UV exposure: to complete the process, the assembly is exposed to UV light at 365 nm for 30 sec to fully cross-link the bottom dry film, effectively bonding the bottom and the top layers. The exposure dose is 450 $mJ\,cm^{-2}$. Cross-linking is also essential as it enhances the mechanical and chemical stability of the dry film, ensuring its durability in microfluidic applications.

Figure 1b presents an exploded view of the chip at the end of the fabrication process, while **Figure 1**c provides a picture of a fabricated physical fluidic chip. The entire fabrication process takes less than 1 h, does not require a cleanroom facility, and allows for an easy tuning of the channel geometry without the need for physical lithography masks. The total cost of materials and reactants per chip is estimated to be only a few cents.

The microchannel geometry strongly influences the gas flow pattern. Therefore, precise characterization of the microchannel's dimensions and geometry is essential before performing mass flow measurements and comparing them with theoretical models. The length and width of the three microchannel samples were measured using an optical microscope with objectives ranging from 0.5 × to 20 × (**Figure 2**a and b). In the images, the blue spots visible in the image are trapped air bubbles, leading to poor adhesion of the dry film and delamination. However, these defects do not affect the functionality of the microchannel, as they have minimal volume and, most importantly, are only connected to the reservoirs. The channel lengths were 11.5 mm as expected. The measurement of the width of the channel provided slightly different results for each sample, that is $W = 193$, 191 and 194 µm for Samples 1, 2 and 3, respectively. The microchannels cross-section is slightly trapezoidal, with the base being approximately 4 µm narrower than

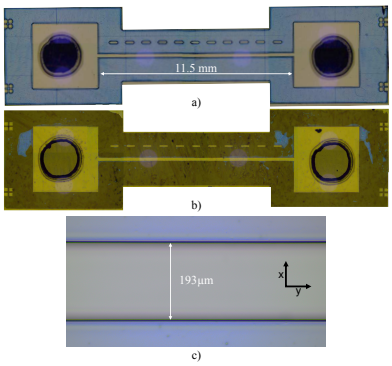

Figure 2. Geometrical characterization of the channel dimensions: a) microscope image of the entire channel after development, captured using a 0.5 × objective, viewed from the bottom (only the top dry film layer is visible); b) the same channel post-sealing with the bottom substrate, showing the entire structure through the transparent top substrate. The blue spots are bonding defects (not affecting performance, as they are not directly connected to the channel); and c) zoomed-in view of the channel width, captured with a 20 × objective (prior to sealing).

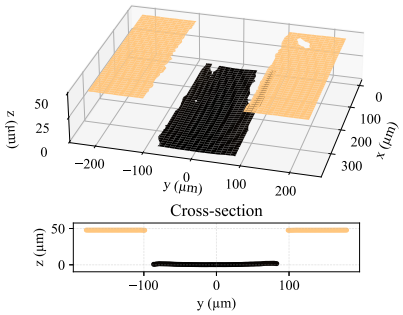

Figure 3. Optical profilometry measurement acquired with a 20 × objective, providing a precise 3D profile of the microchannel's surface topography. This technique effectively captures the microchannel's height; however, it is limited in accurately measuring the steep lateral walls.

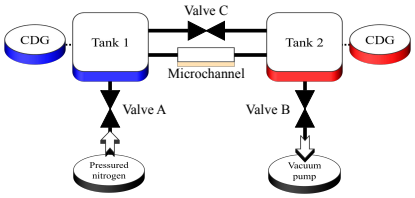

Figure 4. Schematic view of the microfluidic setup implementing the constant volume technique. *CDG: Capacitance Diaphragm Gauge*.

the top. Therefore, the recorded widths represent the channels' width at half-height. The uncertainty in the width measurement, due to the manual measurement process, is estimated to be ± 2 µm. The slight difference between the imposed digital mask channel width of 200 µm and the final fabrication result can be attributed to variations in UV light focusing and diffraction during exposure.

The height of the microchannel is measured at multiple locations along the channel using optical profilometry (**Figure 3**), which determines the thickness of the dry film layer. The height uncertainty, estimated from the reproducibility across different locations, is approximately ± 0.5 µm. The measurements provide dimensions of $H = 46.9$, 48.2 and 47.1 µm, for Samples 1, 2 and 3, respectively. It is to note that the width of the microchannel cannot be measured accurately using profilometry, as the technique struggles with steep slopes, which is the case in the vicinity of the side walls of the microchannel.

Each sample's dimensions are measured before sealing to establish the relationship between gas flow and channel geometry. After sealing, a visual inspection is performed under optical microscope to check for delamination, trapped air bubbles, or any obstacles along the microchannels, ensuring that they are free of contaminants.

To measure the characteristics of the gas flow through the microchannel, we used an experimental fluidic setup that implements the constant volume technique[29,30].This technique is commonly employed in the literature for micro-channels and gas/surface interactions characterization.[31–33] The experimental setup is illustrated in **Figure 4**. The input and output ends of the microchannel are connected to two tanks with volumes $V_1 = 88.7 \pm 1.6$ mL and $V_2 = 56.1 \pm 0.4$ mL, respectively. Each tank is equipped with a capacitance diaphragm gauge (CDG) for real-time pressure measurement. The CDGs have a full scale of 1.33 bar with an accuracy of 0.2 % on reading, and an acquisition frequency of up to 33 Hz. Valves A and B connect the tanks to a pressurized nitrogen bottle and a vacuum pump, respectively, while Valve C directly connects the tanks, allowing for immediate pressure equalization across the setup.

Connecting the chip to the microfluidic setup without causing leakage presents a significant challenge. We have tested clamping solutions but our observations indicate a clear reduction in the dry film thickness when a clamping force was applied. To address this issue, we opted for a two-step gluing process using Polyether-Ether-Ketone (PEEK) tubes to connect the chip to the setup. First, two short PEEK tubes with an outer diameter of 2 mm were glued into the holes in the top PMMA substrate using vacuum-grade Araldite® glue. Once the glue hardened, larger PEEK tubes with an inner diameter of 2 mm were glued over the smaller tubes, resulting in the assembly shown in **Figure 5**. These tubes are permanently connected to the microfluidic setup at their other ends using standard metallic ferrule connectors and Swagelok® tube fittings. This method provides a quick and reliable way to connect the chip, ensuring no mechanical stress on the microchannel while achieving leak tightness.

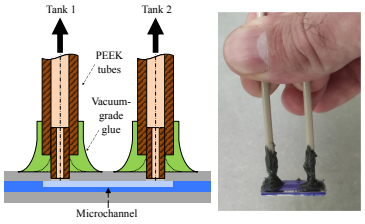

Figure 5. Schematic cross-sectional view and picture of the chip connection to the microfluidic setup. Inner and outer PEEK tubes are glued using Araldite® glue.

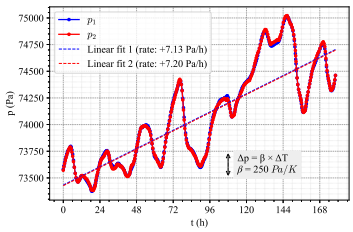

Figure 6. Leakage tests conducted at equilibrium pressure for approximately one week, with Tanks 1 and 2 disconnected. The pressure variation due to a temperature variation of 1 K is indicated by the black arrow.

The leak rate of the entire setup was evaluated by monitoring the pressure over the course of about a week, as shown in **Figure 6**. The pressure variation rate measured in the two tanks were 7.13 $\mathrm{Pa\,h^{-1}}$ and 7.20 $\mathrm{Pa\,h^{-1}}$, respectively. This experiment has been performed repeatedly six times with reproducible results, yielding leak rates consistently below 10 $\mathrm{Pa\,h^{-1}}$. The observed pressure oscillations are attributed to a temperature variation of approximately ± 2 °C caused by the day/night cycle. Despite the air conditioning maintaining a steady temperature in the experimental room, daytime sunlight exposure may still cause slight temperature variations in the setup. The pressure increase due to temperature variations, leak or out-gassing, corresponds to a flow rate which is negligible compared to the flow rate through the microchannel induced by the pressure disequilibrium, and can be accounted for in post-processing of the data. Analogously, the temperature oscillations can be considered as negligible

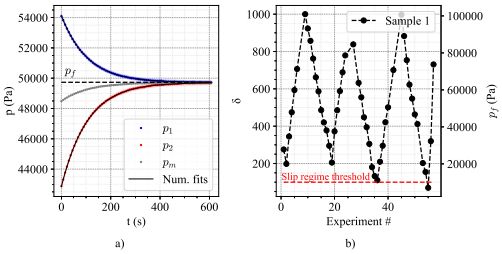

Figure 7. Experimental pressure conditions in the microfluidic channel, at a temperature maintained constant at 21 °C: a) pressure evolution in both tanks during one experiment, starting from an initial pressure difference and progressing until equilibrium is reached. The mean pressure is indicated by the gray curve. The black curves represent the fits provided by **Equation 2**; b) variation of the final rarefaction parameter in the microchannel of Sample 1 across successive experiments with various pressure conditions. The corresponding equilibrium pressure is indicated on the right-hand side axis.

during the time of one experiment, that is less than 10 min.

Calculations of the hydraulic resistance of the microchannel, reservoirs, and smaller PEEK tubes were realized to ensure that the pressure drop between the CDG in both tanks and the inlet or outlet of the micro-channel is negligible, which could otherwise affect the constant volume technique implementation. Hydraulic resistances for channels with rectangular and circular cross-sections can be computed using standard fluid mechanics theory.[34] Our results indicate that the hydraulic resistance of the microchannel is more than 200 times higher than that of the reservoirs and nearly 10^4 times higher than that of the PEEK tubes. The remaining components of the microfluidic setup, having even larger cross-sections, exert a negligible influence. Therefore, we can confidently conclude that the conductance measurements obtained in this work were influenced by the microchannel's geometry solely.

Gas flows through a microchannel when a pressure difference is applied between its inlet and outlet. Thus, the experiment consisted in imposing an initial state of pressure difference between the inlet and outlet of the microchannel, and then observing the pressure evolution in both tanks until a final equilibrium state is reached (equal pressure in both tanks). Since Valves A, B and C are closed during the process (**Figure 4**), the relaxation process occurs due to gas mass transport through the microchannel only. The initial pressure difference can be imposed either by injecting pressurized nitrogen into Tank 1 or by vacuuming Tank 2.

Through the gas equation of state it is possible to relate the mass variation to the pressure variation in the tank. By monitoring the pressure in both tanks, the mass flow rate $\dot{m}$ through the microchannel can be computed as follows for an isothermal tank:

$$\dot{m}_i = \frac{V_i}{R_s T}|\dot{p}_i| \tag{1a}$$

where subscript i refers to Tank 1 or 2, $\dot{p}_i$ is the time derivative of pressure, R_s is the specific gas constant, and T is the temperature. Temperature measurements are obtained via a thermometer in the room, and observed fluctuations are minimal, exerting a negligible effect on the reproducibility of the experiments. The mass flow rate can also be calculated using the pressure difference between the tanks:

$$\dot{m}_\Delta = \frac{V_{eq}}{R_s T}|\dot{p}_1 - \dot{p}_2| \tag{1b}$$

where $V_{eq} = (V_1 V_2)/(V_1 + V_2)$ is the equivalent volume. During a single experiment the temperature is constant 21 ± 1 °C. Due to the mass conservation law (neglecting the microchannel volume compared to the tanks'), the measurements of $\dot{m}_1$, $\dot{m}_2$ and $\dot{m}_\Delta$ should yield the same result.[29,30]

A typical experiment of pressure variation with time relaxing to equilibrium is illustrated in **Figure 7**a. To validate the consistency of the experimental pressure variation data with the theoretical model, the data is fitted using the equation proposed in Silva *et al.*,[30] which is expressed as follows:

$$p_i = \frac{\Psi_A}{\exp(\frac{t}{\tau}) + \Psi_B} + p_f \tag{2}$$

where p_f is the equilibrium pressure, and the only fitting parameters are the equilibrium time constant τ, and constants Ψ_A and Ψ_B which are directly related to the conductance of the channel, and hence depend on the channel geometry.

The experimental campaign consisted in performing experiments for several rarefaction conditions of the flow, which can be measured via the rarefaction parameter, denoted as δ_m, defined as:

$$\delta_m = \frac{p_m L}{\mu\sqrt{2R_s T}} \tag{3}$$

where $p_m = (p_1 + p_2)/2$ is the average pressure inside the microchannel, and μ is the dynamic viscosity of the gas. Let us note that, due to the volume difference between V_1 and V_2 in our constant-volume setup, the average pressure, and thus the rarefaction parameter, varies as the pressures in the tanks equalize, resulting in multiple rarefaction conditions during a single experiment (**Figure 7**a). The pressure conditions tested in this work range from sub-atmospheric down to approximately 10^4 Pa, which match with rarefied gas conditions in the slip regime threshold. Pressure cycles were conducted to check for any permanent deformation or hysteresis effects on the microchannel dimensions, in order to confirm that the materials used can withstand low-pressure conditions without deformation (**Figure 7**b). Multiple samples were tested over several days to assess the reproducibility of the fabrication process and the reliability of the microfluidic characterization over extended periods. As will be explained in the following paragraphs, the channels withstood various low-pressure test cycles, resulting in reproducible measurements.

As presented in **Figure 8**, the mass flow rate was measured by following the pressure variation with time in either tank (**Equation 1a**), or the pressure difference with time between both tanks (**Equation 1b**). The results are presented for three different values of the rarefaction parameter δ, which span from slip regime until hydrodynamic regime. From these

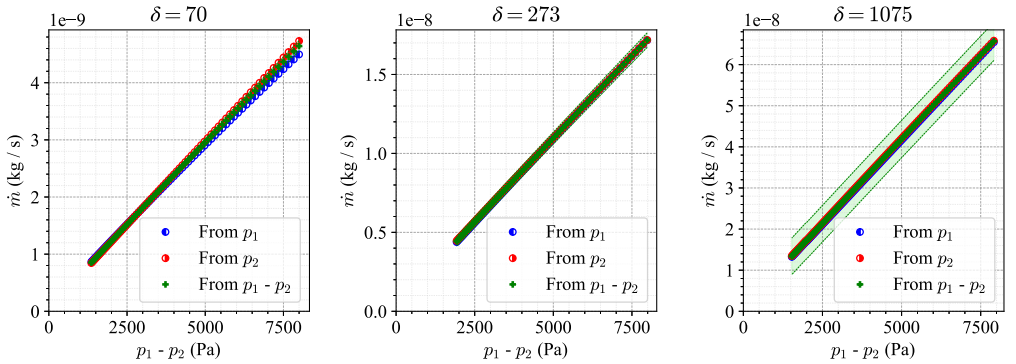

Figure 8. Mass flow rate as a function of pressure difference across the microchannel, for three different rarefaction parameters δ. The results are derived from the pressure variation with time (**Figure 7**a) by using **Equation 1a** and **Equation 1b**. The shaded regions indicate the uncertainty in the mass flow rate (the method for computing uncertainty is described in Rojas-Cárdenas *et al.*[29]).

plots one can appreciate the quality of the obtained results, since the three independent measurements realized for each experiment give almost superposed results. The agreement between these measurements shows that the methodology is consistent with the mass conservation law. Furthermore, it is possible to see from these results that the experimentally imposed mass flow rates differed by several order of magnitudes through the microdevice in the different experiments, that is from 10^{-9} kg/s to almost 10^{-7} kg/s. This proves that the fabrication technique is suitable for a wide range of microfluidic applications were different flow rates are needed at different rarefaction levels.

The experimental measurements of mass flow rate were compared to the model of Ebert and Sparrow,[35] for flows in rectangular cross-section channels for slightly rarefied conditions:

$$\dot{m}_{th} = \frac{H^4}{4aL}\frac{p_2^2}{\mu R_s T}\left[a_1\frac{\left(\frac{p_1}{p_2}\right)^2-1}{2}+a_2\left(\frac{p_1}{p_2}-1\right)Kn\right] \quad (4)$$

where $a = H/W$ is the microchannel's cross-section aspect ratio, a_1 and a_2 are dimensionless coefficients that depend on the aspect ratio and the tangential momentum accommodation coefficient,[4,30] and $Kn = 2/(\sqrt{\pi}\delta_m)$ is the mean Knudsen number within the microchannel. This model is based on the first-order slip boundary condition and is valid only when $Kn < 0.01$, which corresponds to a lower limit for the average pressure of approximately 10^4 Pa in our case. Using **Equation 4**, one can compare the experimental and theoretical data for the analyzed microchannel under any given pressure conditions, provided its dimensions are known.

Rather than using the mass flow rate to compare the different experiments, it is more meaningful to consider the conductance of the channel, which is independent of the imposed pressure difference and the gas composition, and can be calculated as follows:

$$C = \frac{\dot{m}R_sT}{p_1 - p_2}. \quad (5)$$

The conductance varies with the mean rarefaction parameter. Since the mean rarefaction parameter of the flow changes slightly during an experiment, the data treatment of pressure variation with time was divided into subsets where the rarefaction parameter fluctuates by less than 1 %. Each subset yields a corresponding conductance value. As can be readily seen from **Figure 8**, the conductance can be determined by the slope of the mass flow rate plotted against the imposed pressure difference. In this figure, the overall conductance value obtained is 3.17×10^{-7} m^3/s, calculated from the average of the slopes of the three curves.

The experimental conductance data for various values of the rarefaction parameter for the three different samples, tested over several days to ensure reproducibility, are presented and plotted in **Figure 9**. This data is compared to theoretical values obtained from Equations 4 and 5. In this pressure range, the theoretical conductance follows a linear relationship with the rarefaction parameter, with the corresponding slope depending on the geometrical properties of the microchannel. The large number of experiments and the excellent agreement between experiments and theoretical model demonstrate the reliability of the channel fabrication process and the experimental methodology. It is thus possible to state that the microchannels were successfully fabricated with accurate dimensional control. Additionally, the consistency of conductance at sub-atmospheric pressures, down to the kPa range, suggests that the microchannel dimensions are unaffected by both low pressure and pressure fluctuations, thereby validating our choice of materials and fabrication process. Overall, these findings confirm the effectiveness of our design and rapid and cost-effective fabrication approach, demonstrating the potential for further applications in microfluidics.

In summary, in this study we developed a low-cost

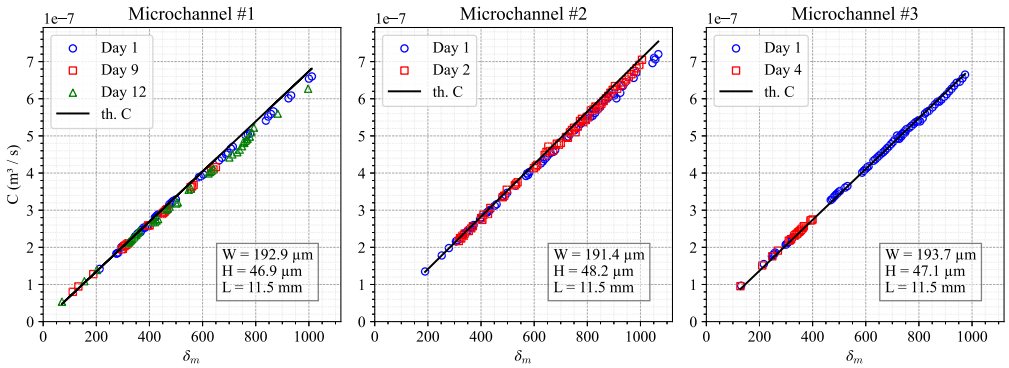

Figure 9. Experimental measurements of conductance for three different microchannels as a function of the rarefaction rate (δ_m) using nitrogen gas, at 21 °C. Each experimental point consists in one single experiment. The dimensions of the microchannels are indicated in the figure (W = width, H = height, L = length). The theoretical conductance, derived from Equations 4 and 5, is represented by the solid black curve on each plot.

method for fabricating microchannels using maskless photolithography and evaluated their performances when submitted to gaseous flows under various rarefaction parameters. Three microchannel samples were fabricated with the following nominal dimensions of height $H = 50\,\mu$m, width $W = 200\,\mu$m and length $L = 11.5$ mm. A thorough discussion on the fabrication materials and methodology used in order to produce these samples was presented. Our findings show that the channel is completely leak tight and that the geometry of the channel is not affected across different pressure levels, indicating that sub-atmospheric conditions do not compromise the microchannel geometry. The rarefaction parameters tested go until slip regime conditions. Our experimental results, validated against theoretical predictions, confirm the accuracy and rapidity of our fabrication process and the reliability of our cost-effective materials. This demonstrates the reliability of our materials and fabrication techniques for applications requiring precise dimensional control with little design efforts. Furthermore, this approach enables rapid and versatile development of custom microchannels, facilitating the optimization of their design and implementation. It is thus possible to state that this fabrication process establishes a robust, time-efficient, low-cost fabrication methodology for rarefied gas flow applications. The samples were fabricated in less than 1 h and the estimated cost, at a laboratory level, was in the order of a few cents (for materials and energy consumption) and the process does not require a clean room facility. These results are significant for accelerating the design and prototyping of cost-effective microfluidic devices, paving the way for developing affordable applications involving rarefied gases, such as Knudsen pumps, gas chromatography devices, volatile organic compounds sensors, fluidic oscillators and more.

This work was carried out with the financial support of the Research Federation FERMaT (FR 3089), Toulouse University and ANR France Relance MIKROFACTORI. The authors would also like to express their thanks to Franz Schweizer for providing data processing scripts and François Guerin for his experimental support.

BIBLIOGRAPHY

[1]Y.-H. Wang, C.-P. Chen, C.-M. Chang, C.-P. Lin, C.-H. Lin, L.-M. Fu, and C.-Y. Lee, "MEMS-based gas flow sensors," Microfluidics and Nanofluidics **6**, 333–346 (2009).
[2]F. Ejeian, S. Azadi, A. Razmjou, Y. Orooji, A. Kottapalli, M. Ebrahimi Warkiani, and M. Asadnia, "Design and applications of MEMS flow sensors: A review," Sensors and Actuators A: Physical **295**, 483–502 (2019).
[3]D. P. Poenar, "Microfluidic and Micromachined/MEMS Devices for Separation, Discrimination and Detection of Airborne Particles for Pollution Monitoring," **10**, 483 (2019), num Pages: 483 Place: Basel, Switzerland Publisher: MDPI AG.
[4]S. Kandlikar, S. Garimella, D. Li, S. Colin, and M. R. King, *Heat Transfer and Fluid Flow in Minichannels and Microchannels*, 2nd ed. (Elsevier, 2014).
[5]A.-G. Niculescu, C. Chircov, A. C. Bîrcă, and A. M. Grumezescu, "Fabrication and Applications of Microfluidic Devices: A Review," International Journal of Molecular Sciences **22**, 2011 (2021), number: 4 Publisher: Multidisciplinary Digital Publishing Institute.
[6]S. M. Scott and Z. Ali, "Fabrication Methods for Microfluidic Devices: An Overview," Micromachines **12**, 319 (2021), number: 3 Publisher: Multidisciplinary Digital Publishing Institute.
[7]J. Charmet, R. Rodrigues, E. Yildirim, P. K. Challa, B. Roberts, R. Dallmann, and Y. Whulanza, "Low-Cost Microfabrication Tool Box," Micromachines **11**, 135 (2020), number: 2 Publisher: Multidisciplinary Digital Publishing Institute.
[8]Y. Fan, "Low-cost microfluidics: materials and methods," Micro & Nano Letters **13**, 1367–1372 (2018), _eprint: https://onlinelibrary.wiley.com/doi/pdf/10.1049/mnl.2018.5169.
[9]N. C. Speller, G. G. Morbioli, M. E. Cato, T. P. Cantrell, E. M. Leydon, B. E. Schmidt, and A. M. Stockton, "Cutting edge microfluidics: Xurography and a microwave," Sensors and Actuators B: Chemical **291**, 250–256 (2019).
[10]D. J. Guckenberger, T. E. d. Groot, A. M. D. Wan, D. J. Beebe, and E. W. K. Young, "Micromilling: a method for ultra-rapid prototyping of plastic mi-

crofluidic devices," Lab on a Chip **15**, 2364–2378 (2015), publisher: The Royal Society of Chemistry.
[11]D. Zhang, G. López-Quesada, S. Bergdolt, S. Hengsbach, K. Bade, S. Colin, and M. Rojas-Cárdenas, "3D micro-structures for rarefied gas flow applications manufactured via two-photon-polymerization," Vacuum **211**, 111915 (2023).
[12]K. Gao, J. Liu, Y. Fan, and Y. Zhang, "Ultra-low-cost fabrication of polymer-based microfluidic devices with diode laser ablation," Biomedical Microdevices **21**, 83 (2019).
[13]N. Xiang, H. Yi, K. Chen, S. Wang, and Z. Ni, "Investigation of the maskless lithography technique for the rapid and cost-effective prototyping of microfluidic devices in laboratories," Journal of Micromechanics and Microengineering **23**, 025016 (2013).
[14]M. Kang, C. Han, and H. Jeon, "Submicrometer-scale pattern generation via maskless digital photolithography," Optica **7**, 1788–1795 (2020), publisher: Optica Publishing Group.
[15]M. Rojas Cardenas, I. Graur, P. Perrier, and J. G. Meolans, "Thermal transpiration flow: A circular cross-section microtube submitted to a temperature gradient," Physics of Fluids **23**, 031702 (2011).
[16]M. Rojas-Cárdenas, I. Graur, P. Perrier, and J. G. Méolans, "Time-dependent experimental analysis of a thermal transpiration rarefied gas flow," Physics of Fluids **25** (2013).
[17]G. López Quesada, G. Tatsios, D. Valougeorgis, M. Rojas-Cárdenas, L. Baldas, C. Barrot, and S. Colin, "Design guidelines for thermally driven micropumps of different architectures based on target applications via kinetic modeling and simulations," Micromachines **10**, 249 (2019).
[18]T. Byambadorj, Q. Cheng, Y. Qin, and Y. B. Gianchandani, "A monolithic si-micromachined four-stage knudsen pump for μgc applications," Journal of Micromechanics and Microengineering **31**, 034001 (2021).
[19]Y. Qin and Y. B. Gianchandani, "A fully electronic microfabricated gas chromatograph with complementary capacitive detectors for indoor pollutants," Microsystems & Nanoengineering **2**, 15049 (2016).
[20]G. Saliba, T. Camps, V. Raimbault, and L. Baldas, "Fabrication of high-frequency microfluidic oscillators with integrated thermal instrumentation," Sensors and Actuators A: Physical **365**, 114844 (2024).
[21]M. V. Pugachev, A. I. Duleba, A. A. Galiullin, and A. Y. Kuntsevich, "Micromask Lithography for Cheap and Fast 2D Materials Microstructures Fabrication," Micromachines **12**, 850 (2021), number: 8 Publisher: Multidisciplinary Digital Publishing Institute.
[22]S. Ostmann and C. J. Kähler, "A simple projection photolithography method for low-cost rapid prototyping of microfluidic chips," Microfluidics and Nanofluidics **26**, 24 (2022).
[23]R. Courson, S. Cargou, V. Conedera, M. Fouet, M. C. Blatche, C. L. Serpentini, and A. M. Gue, "Low-cost multilevel microchannel lab on chip: DF-1000 series dry film photoresist as a promising enabler," RSC Adv. **4**, 54847–54853 (2014).
[24]K. J. Zhong, Y. Q. Gao, and F. Li, "Maskless Lithography Based on DMD," Key Engineering Materials **552**, 207–213 (2013).
[25]Z. Wang, W. Yang, Y. Qin, W. Liang, H. Yu, and L. Liu, "Digital micromirror device -based light curing technology and its biological applications," Optics & Laser Technology **143**, 107344 (2021).
[26]R. M. Guijt and M. C. Breadmore, "Maskless photolithography using UV LEDs," Lab on a Chip **8**, 1402–1404 (2008), publisher: The Royal Society of Chemistry.
[27]D.-H. Dinh, H.-L. Chien, and Y.-C. Lee, "Maskless lithography based on digital micromirror device (DMD) and double sided microlens and spatial filter array," Optics & Laser Technology **113**, 407–415 (2019).
[28]S. Haldar, G. Vashisht, U. K. Ghosh, A. K. Jaiswal, S. Porwal, A. Khakha, T. K. Sharma, and V. K. Dixit, "Development of a simple cost-effective maskless-photolithography system," AIP Conference Proceedings **2115**, 030219 (2019).
[29]M. Rojas-Cárdenas, E. Silva, M.-T. Ho, C. J. Deschamps, and I. Graur, "Time-dependent methodology for non-stationary mass flow rate measurements in a long micro-tube," Microfluidics and Nanofluidics **21**, 86 (2017).
[30]E. Silva, C. J. Deschamps, M. Rojas-Cárdenas, C. Barrot-Lattes, L. Baldas, and S. Colin, "A time-dependent method for the measurement of mass flow rate of gases in microchannels," International Journal of Heat and Mass Transfer **120**, 422–434 (2018).
[31]E. B. Arkilic, K. S. Breuer, and M. A. Schmidt, "Mass flow and tangential momentum accommodation in silicon micromachined channels," Journal of Fluid Mechanics **437**, 29–43 (2001).
[32]T. Ewart, P. Perrier, I. Graur, and J. G. Méolans, "Tangential momemtum accommodation in microtube," Microfluidics and Nanofluidics **3**, 689–695 (2007).
[33]J. Pitakarnnop, S. Varoutis, D. Valougeorgis, S. Geoffroy, L. Baldas, and S. Colin, "A novel experimental setup for gas microflows," Microfluidics and Nanofluidics **8**, 57–72 (2010).
[34]H. Bruus, *Theoretical Microfluidics* (Oxford University Press, 2007) google-Books-ID: wQxREAAAQBAJ.
[35]W. A. Ebert and E. M. Sparrow, "Slip Flow in Rectangular and Annular Ducts," Journal of Basic Engineering **87**, 1018–1024 (1965).